Comparing Digital Implementations of Torque Control for BLDC Motors with Trapezoidal Back-Emf

Edmundo Pozo Fortunić[1], Abdalla Swikir[123], Saeed Abdolsah[1] and Sami Haddadin[12]

***Abstract*— This paper gives a systematic comparison between the digital implementations of two current state-of-the-art control techniques for Brushless DC Motors (BLDC) with trapezoidal back-emf, namely Six-Step-Commutation (6SC) and Modified Field Oriented Control (MFOC). Ideally, both techniques are able to produce ripple-free torque. However, due to several real-world factors, including discrete implementation and requirements on fundamental-to-sampling frequency ratio, this is not possible in reality. Based on continuous PI-controllers and their discrete approximations, including a delayed version, we compare the performance of 6SC and MFOC based on the torque ripple and the mean torque error. Conclusively, with the use of the continuous PI controllers and MFOC it is indeed possible to generate smooth torque also over high dynamic ranges, which so far was only clear for low speeds. Still, for the discrete PI control case, ripple-free torque is not achievable, though it is apparent that the generated ripple is significantly lower than those of 6SC with continuous or discrete implementation. For torque tracking, the error increases disproportionally for 6SC compared to MFOC.**

I. Introduction

Brushless DC motors (BLDC) and Surface Mount Permanent Magnet Synchronous Motors (PMSM) have been incorporated to Robotics for many years now. Their advantage over brushed DC motors for durability and higher power-to-weight density have made a rise to popularity in many applications [1][2]. These two motors differ in their manufacturing. The BLDC is characterized by a trapezoidal shape back-emf phase voltage, while the PMSM is driven towards a sinusoidal one [3]. Common BLDC applications have focused on using Six-step Commutation (6SC) control technique by energizing two phases of the motor to generate torque while commutating the selected phases along the rotor angle. This technique treats the BLDC as a DC motor over each commutation step and is sufficient for most applications focused on position or speed control. However, the current and torque ripples generated at each commutation makes it unreliable for smooth torque operation and subsequent applications [4]. On the other hand, using Field Oriented Control (FOC) over PMSMs allows the implementation of a rotating reference frame that enables control of the torque with a good dynamic performance and no ripple, which is very well suited for higher level applications within robotics such as impedance control for dynamic compliant robots [5]. A problem comes to surface in highly compact and integrated robotic applications such as hands or prostheses because small enough PMSMs are not available at the market. BLDCs should be the closest alternative, however, since a smooth torque control is not yet guaranteed, most designs still use DC- or low-power piezo-motors [6].

For an optimal solution, several methods have been proposed [7]. One is a modified FOC (MFOC) [3] [8] [9], where a new oscillating reference frame provides a direct relation with the torque using a pseudo-park transformation matrix [10]. Additional variations have been proposed based or derived from the same principle [11] [12]. The mathematical analysis has been properly developed, simulated and implemented with good results. However, these simulations were developed in continuous-domain and implemented at low operational speeds and steady states, using BLDC motors for continuous operation. By doing so, the fact that digital systems are actually discrete can be neglected due to a very high sampling-to-fundamental frequency ratio and the continuous analysis retains its good behaviour. Be that as it may, these approximations are not feasible within motors that require a higher dynamic operational speed range as within robotics. At higher speeds, the electrical frequency of the currents and voltages increase, consequently the fundamental-to-sampling frequency ratio of the system decreases, and inaccuracies between the continuous domain simulation and discrete implementation are generated.

Some of these effects were simulated in [13], where the torques of motors operating at high speeds using 6SC and FOC were compared. A decrease over the mean torque and an increase in torque ripple is highly noted in both techniques. Although an overall architecture of the simulated system is presented and a discrete architecture of the controllers is inferred, no additional information on the discrete nature, mathematical model of the controllers nor the tuned parameters are presented.

The specific contributions of this work addresses this missing analysis by i.) the quantitative comparison of MFOC against 6SC in terms of torque smoothness for both continuous and discrete implementations and ii.) deriving the maximum control gains of state-of-the-art discrete PI control based on the understanding of the minimum fundamental-to-sampling ratio required.

This work was supported by the European Union's Horizon 2020 research and innovation programme as part of the project SoftPro under grant no. 688857 and Darko under grant no. 101017274 and by the German Research Foundation (DFG, Deutsche Forschungsgemeinschaft) as part of Germanys Excellence Strategy EXC 2050/1 Project ID 390696704 Cluster of Excellence Centre for Tactile Internet with Human-in-the-Loop (CeTI) of Technische Universitt Dresden.

[1] The authors are with the Chair of Robotics and Machine Intelligence, MIRMI - Munich Institute of Robotics and Machine Intelligence, Technical University Munich (TUM), D-80797 Munich, Germany [2] and also with the Centre for Tactile Internet with Human-in-the-Loop (CeTI) and [3] with the Department of Electrical and Electronic Engineering, Omar Al-Mukhtar University (OMU), Albaida, Libya (e-mail: edmundo.pozo@tum.de)

The standard modeling and continuous control of a BLDC using both techniques are summarized in Section II. In Section III, the tuning of the continuous controllers is calculated over the system parameters, and two discrete controllers (with and without computational delay) are calculated using the Tustin approximation. Simulation results are evaluated in Section IV. Finally, Section V gives our conclusions.

II. Modeling and Control Background

Since in previous works on MFOC and 6SC [3] [8] [9] various incomparable variants were implemented - some of them with certain simplifications - we summarize the modeling and control such that a common and consistent basis serves our analysis and argumentation and reproducibility of our results.

A. Standard BLDC Motor Modeling

The standard electrical model of the BLDC motor in the stationary abc-reference frame is given by [10]

$$\frac{d}{dt}\begin{bmatrix} i_a \\ i_b \\ i_c \end{bmatrix} = -\frac{R}{L}\begin{bmatrix} i_a \\ i_b \\ i_c \end{bmatrix} + \frac{1}{L}\left(\begin{bmatrix} v_a \\ v_b \\ v_c \end{bmatrix} - \begin{bmatrix} e_a(\theta_e) \\ e_b(\theta_e) \\ e_c(\theta_e) \end{bmatrix}\right), \quad (1)$$

where i_a, i_b and i_c are the phase currents, v_a, v_b and v_c are the input phase to neutral voltages, R and L are the stator phase resistance and inductance, θ_e is the electrical angle of the rotor stated as

$$\theta_e = n_p\theta,$$

where n_p is the number of pole pairs and θ is the rotor angle. e_a, e_b and e_c are the back-emf voltages given by

$$\begin{bmatrix} e_a(\theta_e) \\ e_b(\theta_e) \\ e_c(\theta_e) \end{bmatrix} = K_e n_p \omega \begin{bmatrix} f(\theta_e) \\ f\left(\theta_e - \frac{2\pi}{3}\right) \\ f\left(\theta_e + \frac{2\pi}{3}\right) \end{bmatrix}, \quad (2)$$

where K_e is the magnetic flux linkage constant, ω is the mechanical speed of the motor, and $f(\theta_e)$ is the back-emf normalized profile given by [9]

$$f(\theta_e) = \frac{12}{\pi^2}\sum_{n=1}^{\infty}\left(\frac{\cos(n\pi)-1}{n^2}\right)\sin\left(n\frac{\pi}{6}\right)\sin(n\theta_e) \quad (3)$$

for a trapezoidal shape. By reducing the expression to the fundamental component, $n = 1$, we get the sinusoidal back-emf of a PMSM as seen in Fig. 1(a). Additionally, the produced electromagnetic torque, τ_e, is defined as [10]

$$\tau_e = \frac{1}{\omega}\begin{bmatrix} e_a(\theta_e) \\ e_b(\theta_e) \\ e_c(\theta_e) \end{bmatrix}^T \begin{bmatrix} i_a \\ i_b \\ i_c \end{bmatrix}, \quad (4)$$

and interacts with the dynamic model of the motor via

$$\frac{d}{dt}\begin{bmatrix} \theta \\ \omega \end{bmatrix} = \begin{bmatrix} 0 & 1 \\ 0 & -\frac{B}{J} \end{bmatrix}\begin{bmatrix} \theta \\ \omega \end{bmatrix} + \begin{bmatrix} 0 \\ \frac{1}{J} \end{bmatrix}(\tau_e - \tau_l), \quad (5)$$

where B, J and τ_l are the friction constant, moment of inertia and load torque, respectively.

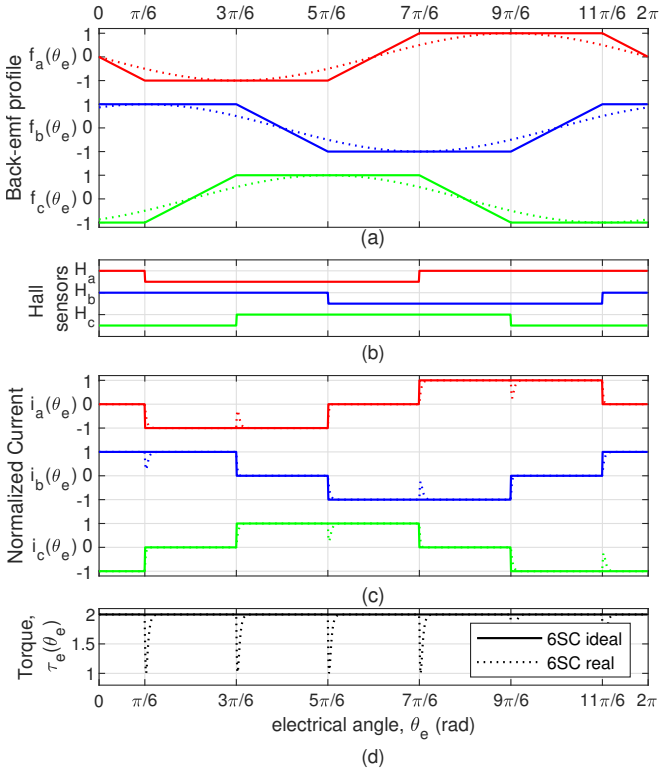

Fig. 1. Six step Commutation control of a BLDC motor over one electrical rotation of phases a (red), b (blue), c (green). (a) Trapezoidal (solid) and sinusoidal (dotted) back-emf profiles in abc-frame. (b) Hall sensors. (c) Ideal (solid) and real (dotted) rectangular current in abc-frame. (d) Torque with ideal (solid) and real (dotted) rectangular currents.

B. Six Step Commutation

This method bases on the commutation of two phases when its corresponding $f(\theta_e)$ has a constant value. Commercially available motors provide embedded Hall sensors in order to detect the commutation steps as seen in Fig. 1(b). For instance, combining (2) with model (1) when $\theta_e \in [\frac{\pi}{6}, \frac{3\pi}{6}]$, the system transfer function simplifies to

$$\begin{aligned} I_{ba}(s) &= H(s)\left(V_{ba}(s) - 2K_e n_p \Omega(s)\right), \\ H(s) &= \frac{1}{2L}\frac{1}{s+\frac{R}{L}}, \end{aligned} \quad (6)$$

where I_{ba}, V_{ba}, Ω and H are the Laplace transforms of the current passing from phases b to a, the voltage between phases b to a, the motor speed, and the transfer function of the motor inductor dynamics, respectively. By doing so, the phase currents ideally become rectangular-shaped, c.f. Fig. 1(c), and produce a ripple free τ_e, see Fig. 1(d), independent of θ_e that could be defined by

$$\tau_e = 2K_e n_p i_{ba}. \quad (7)$$

To establish a control framework for τ_e, a proportional integral (PI) current controller with transfer function

$$G_{PI}(s) = \frac{V_{PI}(s)}{I^*_{ba}(s) - I_{ba}(s)} = K_p\frac{(s+T_i)}{s} \quad (8)$$

is used, where K_p and T_i are the proportional gain and integral time constant, respectively. A $T_i = R/L$ is selected

to cancel the pole in (6), and a feed-forward voltage

$$V_{ff}(s) = 2K_e n_p \Omega(s) \tag{9}$$

is used to compensate for the back-emf voltage. The set-point variables are determined with the * symbol. We thus obtain a closed-loop first order system

$$H_{cl}(s) = \frac{T_e(s)}{T_e^*(s)} = \frac{I_{ba}(s)}{I_{ba}^*(s)} = \frac{K_p}{L_{eq}s + K_p}, \tag{10}$$

where T_e is the Laplace transfom of τ_e and $L_{eq} = 2L$. As a first order system, the bandwidth BW and settling time t_s, with a 1% error, are simply given by

$$BW = \frac{K_p}{2\pi L_{eq}}, \; t_s = \frac{L_{eq}}{K_p} \ln\left(\frac{1}{0.01}\right) \tag{11}$$

and can thus be tuned up by K_p.

C. Modified Field Oriented Control

The principle of FOC is based on the change of the system vectors $X = v, i, f$ or e from the static abc-reference frame X_{abc} as given in (1) to a rotating dq-reference frame representation X_{dq0} [9] via

$$X_{dq0} = T_p(\theta_e) T_c X_{abc}, \tag{12}$$

$$X_{abc} = T_c^{-1} T_p^{-1}(\theta_e) X_{dq0}, \tag{13}$$

$$T_c = \frac{2}{3}\begin{bmatrix} 1 & -\frac{1}{2} & -\frac{1}{2} \\ 0 & \frac{\sqrt{3}}{2} & -\frac{\sqrt{3}}{2} \\ \frac{1}{2} & \frac{1}{2} & \frac{1}{2} \end{bmatrix}, \tag{14}$$

$$T_p(\theta_e) = \begin{bmatrix} \cos\theta_e & \sin\theta_e & 0 \\ -\sin\theta_e & \cos\theta_e & 0 \\ 0 & 0 & 1 \end{bmatrix}, \tag{15}$$

where T_c and $T_p(\theta_e)$ are the Clarke and Park transformation matrixes. As seen in Fig. 2(a), the sinusoidal back-emf profiles in the new reference frame $f_{dq0}(\theta_e) = [f_d(\theta_e), f_q(\theta_e), f_0(\theta_e)]^T$ are simplified to $[0, 1, 0]^T$. This allows us to reduce the number of control variables, and simplify the representation of the back-emf. Moreover, by applying (13) to (4), a control reference of τ_e can be provided without θ_e dependencies with the new reference frame variables as

$$\begin{aligned} \tau_e &= \frac{1}{\omega}\left[T_c^{-1}T_p^{-1}\begin{bmatrix} 0 \\ 1 \\ 0 \end{bmatrix}\right]^T \left[T_c^{-1}T_p^{-1}\begin{bmatrix} i_d \\ i_q \\ 0 \end{bmatrix}\right] \\ &= \frac{3}{2}K_e n_p i_q. \end{aligned} \tag{16}$$

Note that for a motor with trapezoidal back-emf, the torque reduces to

$$\tau_e = \frac{3}{2}K_e n_p (f_d(\theta_e) i_d + f_q(\theta_e) i_q),$$

where a dependency over θ_e is still present due to the oscillating values of f_q and f_d, thus making FOC insufficient for controlling τ_e over i_q only, see Fig. 2(b). To compensate

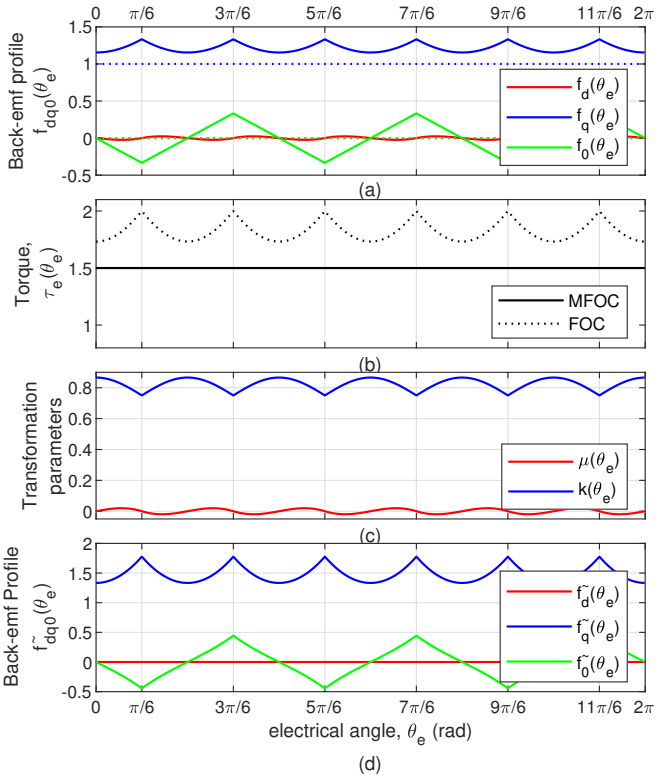

Fig. 2. (a) Trapezoidal (solid) and sinusoidal (dotted) back-emf in rotating dq-frame. (b) Output torque using MFOC (solid) and FOC (dotted) with trapezoidal back-emf and $i_d = 0$ and $i_q = 1$.(c) Parameters $\mu(\theta_e)$ and $k(\theta_e)$ (d) Trapezoidal back-emf in oscillating $dq^{\sim}$-frame.

for this, MFOC defines a new Pseudo-Park transformation matrix

$$\tilde{T}_p(\theta_e) = \frac{1}{k(\theta_e)}\begin{bmatrix} \cos(\theta_e + \mu(\theta_e)) & \sin(\theta_e + \mu(\theta_e)) & 0 \\ -\sin(\theta_e + \mu(\theta_e)) & \cos(\theta_e + \mu(\theta_e)) & 0 \\ 0 & 0 & 1 \end{bmatrix} \tag{17}$$

where μ and k are the transformation parameters, see Fig. 2(c), defined as

$$\mu(\theta_e) = -\tan^{-1}\frac{f_d(\theta_e)}{f_q(\theta_e)}, \; k(\theta_e) = \frac{1}{\sqrt{f_q^2(\theta_e) + f_d^2(\theta_e)}}. \tag{18}$$

Consequently, we now have a new reference frame $\tilde{X}_{dq0}$ given by

$$\tilde{X}_{dq0} = \tilde{T}_p(\theta_e) T_c X_{abc} \tag{19}$$

$$X_{abc} = T_c^{-1} \tilde{T}_p^{-1}(\theta_e) \tilde{X}_{dq0}. \tag{20}$$

The back-emf in the new frame is given as $\tilde{f}_{dq0}(\theta_e) = [0, \frac{1}{k^2(\theta_e)}, \tilde{f}_0(\theta_e)]^T$ as seen in Fig. 2(d). As a result, τ_e is now expressed as

$$\begin{aligned} \tau_e &= \frac{3}{2}K_e n_p k^2(\theta_e)\begin{bmatrix} 0 \\ \frac{1}{k^2(\theta_e)} \\ \tilde{f}_0(\theta_e) \end{bmatrix}^T \begin{bmatrix} \tilde{i}_d \\ \tilde{i}_q \\ 0 \end{bmatrix} \\ &= \frac{3}{2}K_e n_p \tilde{i}_q. \end{aligned} \tag{21}$$

Applying (19) and (20) to (1), gives us

$$\frac{d}{dt}\begin{bmatrix}\tilde{i}_d\\ \tilde{i}_q\\ 0\end{bmatrix} = \frac{1}{L}\begin{bmatrix}\tilde{v}_d\\ \tilde{v}_q\\ \tilde{v}_0\end{bmatrix} - \frac{K_e n_p \omega}{L}\begin{bmatrix}0\\ \frac{1}{k^2(\theta_e)}\\ \tilde{f}_0(\theta_e)\end{bmatrix} - \begin{bmatrix}\frac{R}{L}+k'(\theta_e) & -\mu'(\theta_e) & 0\\ \mu'(\theta_e) & \frac{R}{L}+k'(\theta_e) & 0\\ 0 & 0 & \frac{R}{L}+k'(\theta_e)\end{bmatrix}\begin{bmatrix}\tilde{i}_d\\ \tilde{i}_q\\ 0\end{bmatrix} \tag{22}$$

$$k'(\theta_e) = \frac{n_p\omega}{k(\theta_e)}\frac{dk(\theta_e)}{d\theta_e},\ \mu'(\theta_e) = n_p\omega\left(\frac{d\mu(\theta_e)}{d\theta_e}+1\right) \tag{23}$$

This is a new reference frame model, where $\tilde{v}_d$, $\tilde{v}_q$, $\tilde{v}_0$, $\tilde{i}_d$ and $\tilde{i}_q$ are the pseudo- direct, quadrature, and neutral voltages, and pseudo- direct and quadrature currents, respectively.

With the use of two PI current controllers, one for $\tilde{i}_q(t)$ and one for $\tilde{i}_d(t)$, with transfer function (8) and new decoupling feed-forward voltages given by

$$\begin{bmatrix}\tilde{v}_{ffd}(t)\\ \tilde{v}_{ffq}(t)\end{bmatrix} = L\begin{bmatrix}k'(\theta_e) & -\mu'(\theta_e)\\ \mu'(\theta_e) & k'(\theta_e)\end{bmatrix}\begin{bmatrix}\tilde{i}_d(t)\\ \tilde{i}_q(t)\end{bmatrix} + Ln_pK_e\omega\begin{bmatrix}0\\ \frac{1}{k^2(\theta_e)}\end{bmatrix} \tag{24}$$

to eliminate coupling between $\tilde{i}_q(t)$ and $\tilde{i}_d(t)$, and the back-emf voltage effects, we obtain two independent closed-loop first order systems similar to (10),

$$H_{cl}(s) = \frac{\tilde{I}_q(s)}{\tilde{I}_q^*(s)} = \frac{\tilde{I}_d(s)}{\tilde{I}_d^*(s)} = \frac{K_p}{L_{eq}s + K_p}, \tag{25}$$

where $L_{eq} = L$. By setting $\tilde{i}_d^* = 0$, we assert controllability of τ_e through $\tilde{i}_q^*$ as defined in (21).

III. Controller Setup and Metrics

In order to establish a proper comparison between both techniques, three architecture types are taken into account: the continuous controllers as defined in the previous section, their discrete approximation, and a delayed discrete approximation. The discrete controllers will help us analyze the effects of discretization with and without delay at high speeds. Therefore, several K_p gains must be tuned up to deliver the maximum performance of each controller. For this, the desired operational range of the motor and system capabilities must be taken into consideration.

A. Operational Range of the Motor

The operational range of the motor can be obtained from the motor and system parameters. The maximum speed and torque are given by:

$$\omega^{\max} = \frac{v_{dc} - 2Ri_n}{2K_e n_p}$$
$$\tau_e^{\max} = 2K_e n_p i_n, \tag{26}$$

where v_{dc} denotes the DC voltage of the system and i_n the motor nominal current[1].

[1]If the manufacturer defines lower values due to mechanical, thermal or safety constrains, these should be considered instead.

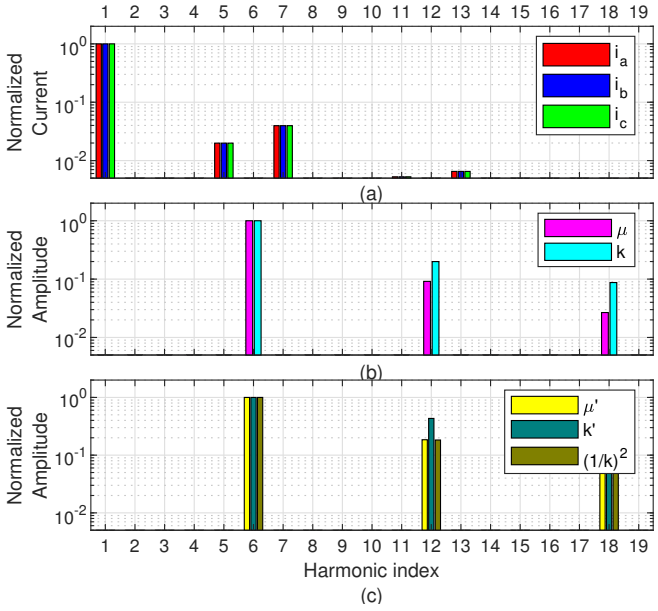

Fig. 3. Normalized Harmonic amplitude index of the first 19^{th} elements. DC component is excluded. (a) Ideal MFOC generated current. (b) Transformation parameters μ (magenta) and k (cyan) (c) Feedforward parameters μ' (yellow) , k' (gray) and $\frac{1}{k^2}$ (brown)

B. Upper bound K_p

1) Continuous Control: Depending on the chosen control techniques K_p has two different upper bounds:

- Six step Commutation: In order to avoid a controller output saturation ($v_{PI} > v_{dc}$) that would affect the linear performance of the closed loop system, a maximum K_p is defined given that the maximum controller input is set to i_n.

$$K_p \leq K_{6\text{SC}}^{\max} = \frac{v_{dc}}{i_n}, \tag{27}$$

- Modified Field Oriented Control: In this technique, the output saturation should not occur in v_{abc}, after applying (20) to the controller outputs, thus a new maximum K_p is defined as

$$K_p \leq K_{\text{MFOC}}^{\max} = \frac{\sqrt{3}}{3}\frac{v_{dc}}{i_n}. \tag{28}$$

2) Discrete control: In the discrete scenario, we first have to define the fundamental-to-sampling ratio as follows. By analyzing the spectrum of the ideal i_{abc} and using the Nyquist criteria, we set a minimum sampling frequency, denoted by $f_s^{\min}$, to acquire the harmonics with more than 1% (7^{th} harmonic), see Fig. 3(a), as

$$f_s^{\min} = 7(2f_e) = 14f_e,$$

where f_e is the fundamental electrical frequency given by

$$f_e = \frac{1}{2\pi}n_p\omega. \tag{29}$$

However, a higher $f_s^{\min}$ is needed for the controller to generate the needed values of k and μ to achieve the $\tilde{X}_{dq0}$ transformation and the required feed-forward terms k', μ' and $\frac{1}{k^2}$, given that their harmonic components have a significant amplitude around the 12^{th} and 18^{th} harmonics too, as seen in

Fig. 3(b). Therefore, a more appropriate minimum sampling-to fundamental ratio is defined as

$$\frac{f_e}{f_s^{\min}} = \frac{1}{36}. \tag{30}$$

Since the sampling frequency of an implemented system, f_s, is limited to the capabilities of the used microcontroller, a new $\omega^{\max}$ would need to be defined using (29) and (30).

- Ideal Discrete Controller: Using the Laplace to Z- transformation of a Zero-Order-Hold (ZOH) system [14], we discretize (6) for 6SC and MFOC and obtain

$$\begin{aligned} H(z) &= (1-z^{-1})\mathcal{Z}\left\{\frac{H(s)}{s}\right\}_{T_s} \\ &= \frac{1}{R_{eq}}\left(\frac{1-e^{-\frac{R}{L}T_s}}{z-e^{-\frac{R}{L}T_s}}\right), \end{aligned} \tag{31}$$

where $T_s = 1/f_s$ and $R_{eq} = 2R$ for 6SC and $R_{eq} = R$ for MFOC. The controller is then discretized using the bi-linear transformation to

$$\begin{aligned} G_{PI}(z) &= K_p\left(1 + \frac{R}{L}\frac{T_s}{2}\left(\frac{z+1}{z-1}\right)\right) \\ G_{PI}(z) &= K_p'\left(\frac{z-z_0}{z-1}\right) \\ K_p' &= K_p\left(\frac{R}{L}\frac{T_s}{2}+1\right), z_0 = \frac{1-\frac{R}{L}\frac{T_s}{2}}{1+\frac{R}{L}\frac{T_s}{2}} \end{aligned} \tag{32}$$

The gain K_p' and pole z_0 of the controller can be approximated using the inverse bi-linear transformation, giving us the final form:

$$G_{PI}(z) = K_p\left(\frac{\frac{R}{L}T_s}{1-e^{-\frac{R}{L}T_s}}\right)\left(\frac{z-e^{-\frac{R}{L}T_s}}{z-1}\right) \tag{33}$$

Combining (31) and (32) results in the closed loop system

$$H_{cl}(z) = \frac{\frac{K_p}{L_{eq}}T_s}{z-1+\frac{K_p}{L_{eq}}T_s}. \tag{34}$$

By maintaining the pole of the system within the unitary circle and positive for a damped response, we obtain the limit for K_p to be

$$K_p \leq K^{\zeta i} = \frac{L_{eq}}{T_s} = L_{eq}f_s. \tag{35}$$

- Delayed Discrete Controller: The previously defined discrete model has not yet taken into account the delay of the controller. Thus a slightly extended controller

$$G_{PI}^d(z) = z^{-1}G_{PI}(z) \tag{36}$$

is introduced, resulting in the closed loop transfer function

$$H_{cl}^d(z) = \frac{\frac{K_p}{L_{eq}}T_s}{z^2-z+\frac{K_p}{L_{eq}}T_s}. \tag{37}$$

TABLE I
SIMULATION PARAMETERS

	Technique		
Parameters	6SC	MFOC	Units
DC Voltage, v_{dc}	24		V
Continuous K_p	36.36	20.99	V/A
Sampling Frequency, f_s	50		kHz
Discrete ideal K_p	36.36	20.99	V/A
Discrete delayed K_p	11.05	5.53	V/A
Nominal Voltage Un	12		V
Rated current i_n	0.66		A
Rated torque τ_e	10		mNm
Phase Resistance R	3.48		Ω
Phase Inductance L	442		μH
Back-emf constant K_e	0.89		$\mathrm{mV/min^{-1}}$
Rotor Inertia J	3.3		$\mathrm{gcm^2}$
Maximum speed $\omega^{\max}$	10000		$\mathrm{min^{-1}}$
Number of pole pairs, n_p	7		

As a second order system, we set a new limit on K_p to obtain a critically damped response and avoid ripple generation as

$$K_p \leq K^{\zeta_d} = \frac{L_{eq}}{4T_s} = \frac{L_{eq}}{4}f_s. \tag{38}$$

Even though $K^{\zeta i}$ and K^{ζ_d} may increase with higher sampling rates, these values cannot exceed $K_{\mathrm{6SC}}^{\max}$ nor $K_{\mathrm{MFOC}}^{\max}$, depending on the selected technique, as it would generate a voltage saturation.

C. Metrics

For quantifying the mean torque error and torque ripple of aforementioned controllers, following torque metrics are introduced.

$$\bar{e}_\tau(\%) = 100|\frac{\bar{\tau}_e}{\tau_e^*} - 1|,\ \tau_r(\%) = 100(\frac{\tau_\sigma}{\tau_e^*}), \tag{39}$$

where $\bar{\tau}_e$ and τ_σ are the mean and standard deviation of τ_e over one electrical period, respectively.

IV. SIMULATION EXPERIMENTS

A. Simulation Settings

A simulation experiment for performance analysis is conducted for the current controllers for nominal current step inputs ($i^* = i_n$ for 6SC and $\tilde{i}_q^* = i_n$ for MFOC). The simulation environment is MATLAB/Simulink with a Runge-Kutta solver at fixed-step of 0.01μs. The Motor 2214S012BXTR (Faulhaber) parameters can be found in Tab. I and are used for evaluating (1) - (5) in double float precision. The trapezoidal back-emf profile $f(\theta_e)$ is calculated until the 19^{th} harmonic given that the amplitudes of higher harmonics are negligible. The motor controllers are simulated using the parameters from Tab. I. Single-float precision was used to emulate the capabilities of commercially available small microcontrollers (μC) with floating point units (FPU). The functions $\sin(\theta_e)$ and $\cos(\theta_e)$, and parameters derived from $f(\theta_e)$ such as μ, k, $d\mu/d\theta_e$ and $dk/d\theta_e$ were calculated and converted to 16bit precision look-up tables (LUTs) with 14bit addressing. This is done to emulate μC implementation and limited memory resources. Controller output voltages were

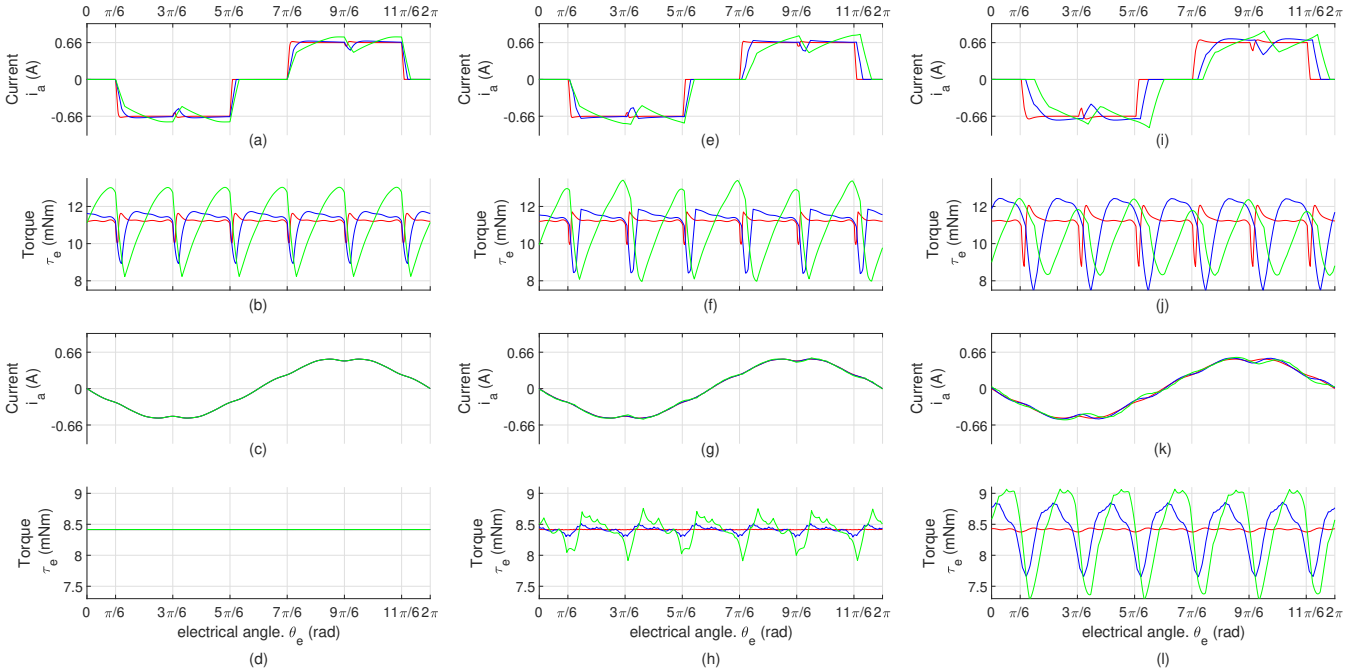

Fig. 4. Simulation results of one electrical rotation at different steady state speeds: 100 rad/s (red), 500 rad/s (blue) and 1000 rad/s (green). With a continuous controller $G_c(s)$: (a) i_a and (b) τ_e using 6SC, and (c) i_a and (d) τ_e using MFOC. With a discrete controller $G_c(z)$: (e) i_a and (f) τ_e using 6SC, and (g) i_a and (h) τ_e using MFOC. With a delayed discrete controller $G_c^d(z)$: (i) i_a and (j) τ_e using 6SC, and (k) i_a and (l) τ_e using MFOC.

simulated as analog signals and not as Pulse Width modulated (PWM) signals to prevent additional ripple generation and extended analysis of its non linearity.

B. Simulation results

Figure 4 shows an electrical cycle of i_a and τ_e at 100, 500 and 1000 rad/s speeds, equivalent to the 9.5%, 47.8% and 95.5% of the maximum speed, using 6SC and MFOC techniques with a continuous, discrete or delayed discrete controller. We first see in (a) 6SC with the continuous controller, where i_a follows the rectangular shaped ideal profile, however, it is limited by the system response and phase commutations. At higher speeds, the current deviates more from the desired reference. These limitations translate in (b) to a fixed τ_e ripple valley around the commutation angles, which increases and becomes wider at higher speeds. On the other hand, MFOC shows in (c) that i_a retains the same shape at all speeds using the continuous controller, and τ_e is shown without ripples in (d). Analyzing the behaviour of 6SC with the discrete controller in (e), we notice that similar distortions occur in i_a as with the continuous controller, which also translate to τ_e ripples in (f). Contrarily, MFOC with the discrete controller start to show in (g) slightly more disturbances in the i_a along the speed increments that translate into quite noticeable τ_e ripples at the mid and high speeds that were not present before. Later on, we see in (i) that 6SC is affected even more with the delayed discrete controller, as the commutation of i_a occurs significantly out of phase as speed increases. This shows in (j) significantly more ripple. Finally, we observe in (k) the behaviour of

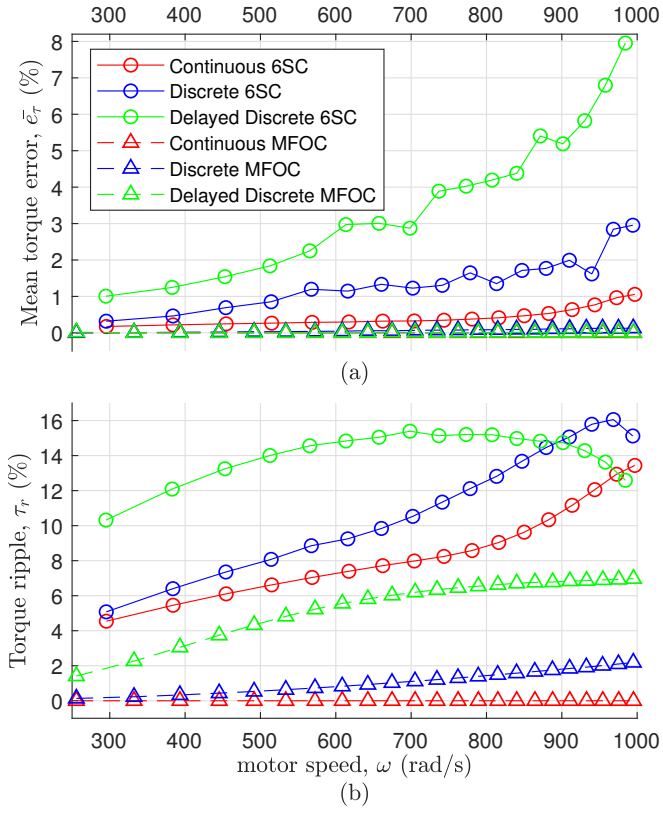

Fig. 5. Evolution of (a) mean torque error and (b) torque ripple over motor speed for 6SC and MFOC techniques using a continuous, discrete and delayed discrete controller.

i_a getting significantly distorted at higher speeds, which translates back to an increase in τ_e ripples in (l), occurring even at low speed.

A quantitative comparison using τ_r, and $\bar{e}_\tau$ is further detailed in Fig. 5. We can see in (a) that $\bar{e}_\tau$ remains close to zero in all instances of MFOC, while it increases with increasing speed in 6SC. On the other hand, the increase of τ_r along the speed is clear in (b) for MFOC with both discrete controllers, and 6SC with all of them. This happens because the fundamental-to-sampling ratio of the system diminishes with the increase of speed. Regardless of this, MFOC has lower τ_r than 6SC with any controller, even with the delayed discrete version, which is the one representing an implementable version of the digital controller.

V. Conclusion

In this paper, it has been confirmed that MFOC can produce a smooth torque output using a continuous controller over the full operational speed range of a BLDC motor. When a delayed discrete controller is used, the resulting mean torque is still maintained but a torque ripple is introduced due to the limitations of the fundamental-to sampling ratio of the system. However, these ripples are significantly lower than the ones produced using 6SC. Since in reality a compromise between maximum speed, sampling frequency and torque ripple is implemented, the ideal continuous controller results cannot be achieved. Still, the well performing ideal discrete MFOC controller could still be asserted by applying standard delay compensation methods.

References

[1] T. Batzel and K. Lee, "Commutation torque ripple minimization for permanent magnet synchronous machines with hall effect position feedback," *IEEE Transactions on Energy Conversion*, vol. 13, no. 3, pp. 257–262, 1998.

[2] S. Derammelaere, M. Haemers, J. De Viaene, F. Verbelen, and K. Stockman, "A quantitative comparison between bldc, pmsm, brushed dc and stepping motor technologies," in *2016 19th International Conference on Electrical Machines and Systems (ICEMS)*, 2016, pp. 1–5.

[3] M. Lazor and M. tulrajter, "Modified field oriented control for smooth torque operation of a bldc motor," in *2014 ELEKTRO*, 2014, pp. 180–185.

[4] S. Sakunthala, R. Kiranmayi, and P. N. Mandadi, "A study on industrial motor drives: Comparison and applications of pmsm and bldc motor drives," in *2017 International Conference on Energy, Communication, Data Analytics and Soft Computing (ICECDS)*, 2017, pp. 537–540.

[5] A. Toedtheide, E. Shahriari, and S. Haddadin, "Tank based unified torque/impedance control for a pneumatically actuated antagonistic robot joint," in *2017 IEEE International Conference on Robotics and Automation (ICRA)*, 2017, pp. 1255–1262.

[6] A. Saudabayev and H. A. Varol, "Sensors for robotic hands: A survey of state of the art," *IEEE Access*, vol. 3, pp. 1765–1782, 2015.

[7] P. Chapman, S. Sudhoff, and C. Whitcomb, "Optimal current control strategies for surface-mounted permanent-magnet synchronous machine drives," *IEEE Transactions on Energy Conversion*, vol. 14, no. 4, pp. 1043–1050, 1999.

[8] A. Lidozzi, L. Solero, F. Crescimbini, and R. Burgos, "Vector control of trapezoidal back-emf pm machines using pseudo-park transformation," in *2008 IEEE Power Electronics Specialists Conference*, 2008, pp. 2167–2171.

[9] P. Kshirsagar and R. Krishnan, "High-efficiency current excitation strategy for variable-speed nonsinusoidal back-emf pmsm machines," *IEEE Transactions on Industry Applications*, vol. 48, no. 6, pp. 1875–1889, 2012.

[10] D. Grenier, L.-A. Dessaint, O. Akhrif, and J.-P. Louis, "A park-like transformation for the study and the control of a nonsinusoidal brushless dc motor," in *Proceedings of IECON '95 - 21st Annual Conference on IEEE Industrial Electronics*, vol. 2, 1995, pp. 836–843 vol.2.

[11] M. A. Amirian, A. Rashidi, S. M. Saghaeian Nejad, and M. Mojiri, "Multiple reference frame control of permanent magnet synchronous motor with non-sinusoidal back emf using adaptive notch filter," in *2015 23rd Iranian Conference on Electrical Engineering*, 2015, pp. 1480–1485.

[12] M. Sumega, P. Rafajdus, S. Kocan, and M. Stulrajter, "Torque ripple reduction in pm motors using current harmonics controller," in *2020 ELEKTRO*, 2020, pp. 1–6.

[13] S. Zossak, P. Varecha, and P. Makys, "Comparison of field oriented and six-step control for high-speed pmsm drive," in *2020 ELEKTRO*, 2020, pp. 1–5.

[14] M. S. Fadali and A. Visioli, "Chapter 3 - modeling of digital control systems," in *Digital Control Engineering (Second Edition)*. Boston: Academic Press, 2013, pp. 165–234.